Evaluation and Mitigation of Rain Effect on Wave Direction and Period Estimation From *X*-Band Marine Radar Images

Zhiding Yang *, Student Member, IEEE*, Weimin Huang ⓘ *, Senior Member, IEEE*, and Xinwei Chen *, Student Member, IEEE*

Abstract—In this article, the accuracy of wave direction and period estimation from *X*-band marine radar images under different rain rates is analyzed, and a simple subimage selection scheme is proposed to mitigate the rain effect. First, each radar image is divided into multiple subimages, and the subimages with relatively clear wave signatures are identified based on the random-forest-based classification model. Then, wave direction is estimated by performing the Radon transform on each valid subimage. As for wave period estimation, a new method is proposed. Texture features are first extracted from each pixel of the selected subimage using the gray-level co-occurrence matrix and combined as a feature vector. Those feature vectors extracted from both rain-free and rain-contaminated training samples are then used to train a random-forest-based wave period regression model. The shore-based *X*-band marine radar images, simultaneous rain rate data, as well as buoy-measured wave data collected on the West Coast of the United States are used to analyze the rain effect on wave parameter estimation accuracy and validate the proposed method. Experimental results show that the proposed subimage selection scheme improves the estimation accuracy of both wave direction and wave period under different rain rates, with reductions of root-mean-square errors (RMSEs) by $6.9°$, $6.0°$, $4.9°$, and $1.0°$ for wave direction under rainless, light rain, moderate rain, and heavy rain conditions, respectively. As for wave period estimation, the RMSEs decrease by 0.13, 0.20, 0.30, and 0.20 s under those four rainfall intensity levels, respectively.

Index Terms—Rain, random forest, subimage selection, wave, *X*-band marine radar.

I. INTRODUCTION

A<small>N</small> *X*-band marine radar plays a significant role in ocean remote sensing taking advantage of its high temporal and spatial resolution. Sea surface variations can be imaged from the backscattering of the electromagnetic waves [1], which makes it possible to utilize the marine radar images to estimate the sea surface features efficiently, such as wind [2], [3], wave [4]–[7],

and current [8]–[10] parameters. The parameters estimated from *X*-band radar data are essential to various coastal activities, such as offshore oil exploitation, ship navigation, and coastal hazard prediction [11], [12]. However, the presence of rainfall will negatively influence the measurement accuracy of those sea state parameters because the raindrops on the ocean surface and in the atmosphere alter both sea surface roughness and *X*-band radar backscatter [13], [14]. In consequence, some wave signatures of radar backscatter images are blurred, and those previously proposed methods for wind and wave parameter estimation might not work well. In order to detect the presence of rain from radar images, various methods have been proposed to classify the radar images into rainless and rain-contaminated types so far, including the mean-and-difference-coefficient-analysis-based method [15], zero-pixel-percentage-based method [2], and the support-vector-machine-based method [16]. Besides, a couple of modified and novel methods for wind parameter estimation with rain mitigation have been proposed, such as the modified-intensity-level-selection-based method [17], the empirical-mode-decomposition-based method [18], and the support-vector-regression-based method [19]. In contrast, two preliminary studies [15], [20] have been conducted for wave parameter estimation using rain-contaminated radar images, and the influence of rainfall intensity on estimation accuracy has never been analyzed.

According to Huang *et al.* [22], for rain-contaminated images, regions that are unaffected or less affected by rainfall can still be used to estimate sea surface parameters. Thus, a novel scheme can be proposed to identify and select regions with clear wave signatures for wave parameter estimation. In [5] and [23], the Radon transform (RT) is applied for wave direction estimation. However, only rainless radar images are used for estimation and analysis. Thus, in order to obtain wave direction information from rain-contaminated radar images, it is reasonable to combine RT-based algorithm with the rainless region identification method. On the other hand, since the texture analysis has already used for the wave height estimation in [24] and [25], it is feasible to extract the texture features from those rainless regions to estimate the wave period. Moreover, machine-learning-based regression algorithms have been applied to estimate the wave height [26], [27] and wind speed [19], [28] from *X*-band marine radar images and receive good results. Hence, it is possible
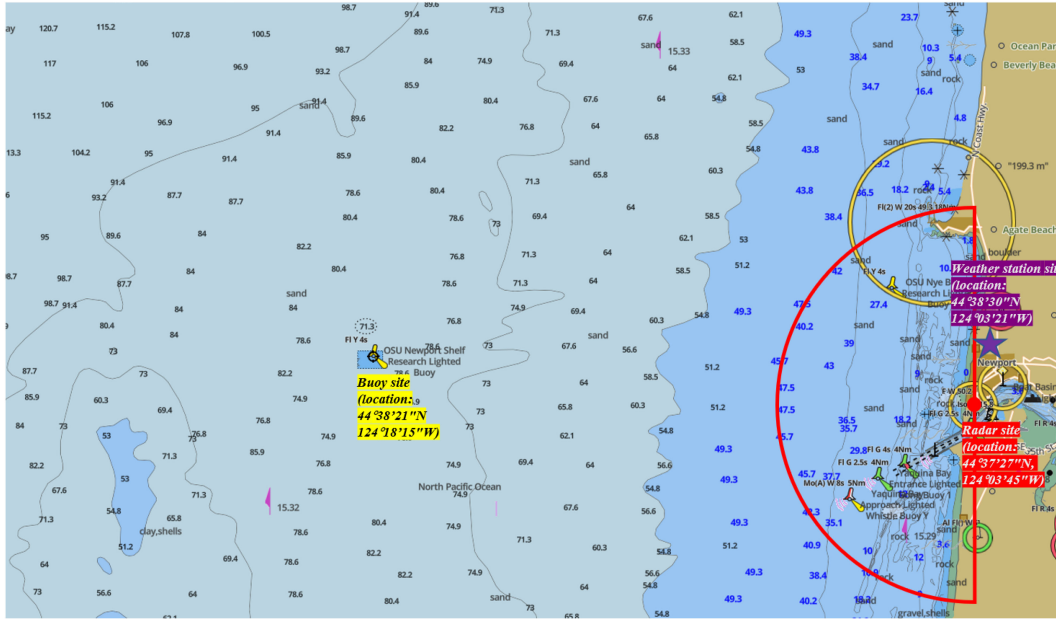
Fig. 1.   Locations of the radar, buoy, and weather station site as well as the bathymetry of the region from GPS Nautical Charts [21].

TABLE I
RADAR INFORMATION

Radar site	A shore-based tower in Newport, OR, USA
Transmit frequency	9.45 GHz
Polarization	Horizontal
Pulse width	80 ns
Range resolution	12 m
Range coverage	3 m - 6087 m
Beam width	0.8°
Azimuth coverage	180°
Antenna height	63 m
Antenna rotation speed	44 rpm
Grey level of radar image	0 - 255

to develop a machine-learning-based model for wave period estimation after extracting the texture features from the selected regions.

In this article, quantitative analysis of the rain intensity on wave direction and period estimation from *X*-band radar data is presented. A subimage selection scheme for identifying the region with relatively clear wave signatures to improve the estimation accuracy and a machine-learning-based wave period measurement method are proposed. In Section II, the radar and environmental data used in this study are described. The proposed methodology is illustrated step by step in Section III. Section IV presents the experimental results as well as rain effect analysis. Finally, Section V concludes this article.

II. DATA OVERVIEW

The radar data used in this study were collected by a commercial *X*-band marine radar (Koden) deployed on a shore-based tower at Yaquina Bay, Newport, OR, USA (44°37′27″N, 124°03′45″W). The information of the radar system is provided in Table I. The range resolution of this radar is 12 m, and the beam width is 0.8°. The resolution of the Cartesian radar image is 5 m. Fig. 1 shows the locations of the radar, buoy, and

weather station site as well as the bathymetry of the region. The coverage of the radar image is shown by a red sector. According to the bathymetry map, the water depths of the observation area range from 0 to 47.5 m. In this study, regions with water depths lower than 10 m are excluded from analysis. The reference wave information is collected per hour by a TriAXYS directional wave buoy located around 20 km from the radar site (44°38′21″N 124°18′15″W). The buoy can measure wave periods of 1.5–30 s with a resolution of 0.1 s. The accuracy of the measured wave period is better than 1%. The buoy measures wave direction from 0° to 360° with a resolution of 1°. The measurement error is within 3°. On the other hand, the hourly average rain rate was recorded every 5 min from a rain gauge with a resolution of 0.1 mm/h and provided by the ARPSWXNET/CWOP weather station (44°38′30″N 124°03′21″W). The measurement error is within 0.5 mm/h. The radar, buoy, and rain gauge instruments are all working 24/7. Since the sampling rates of both buoy and rain gauge are lower than that of the radar, the reference wave and rain data for each radar image are obtained from the closest measurements before or after the image acquisition time. The radar images used for this study were selected between January 11 and July 18, 2019 under a wide range of rain rates. Among those images, 70% of them are randomly selected for training, while the other 30% are used for testing.

III. METHODOLOGY

The overall framework of wave direction and period estimation in this study is presented in Fig. 2.

A. Subimage Selection

Fig. 3 shows examples of radar images obtained under four different rainfall intensities. It can be observed that wave signatures will be affected in different degrees under different rain rates. Specifically, a rain-free radar image is presented in
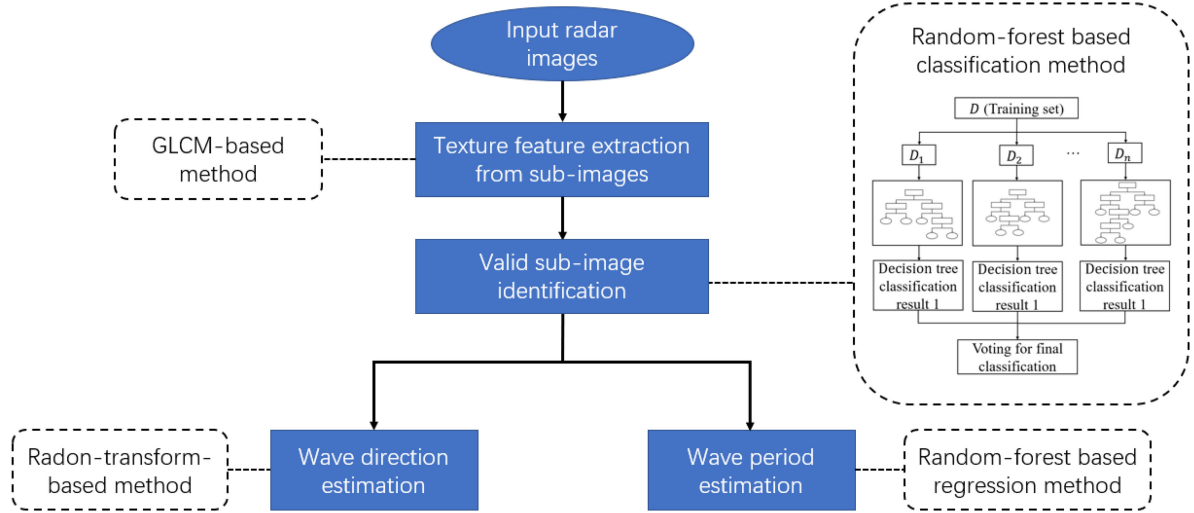
Fig. 2. Framework of wave direction and period estimation.

Fig. 3(a), and the texture of wave signatures can be clearly observed in most of the sea surface regions. In comparison, Fig. 3(b)–(d) shows radar images with blurry wave signatures obtained under rain rates of 1.5, 3.0, and 9.1 mm/h, respectively. It can be found that as the rain rate increases, the proportion of regions dominated by rain echoes increases as well. Nevertheless, for some rain-contaminated images, wave signatures might still be visible in some regions, from which wave parameters can be estimated [22]. On the other hand, regions dominated by rain echoes should be discarded. In order to identify those regions with visible wave signatures, 15 subimages with equal size are first extracted from each radar image, as shown in Fig. 4. For each subimage, texture features are extracted and input into a random-forest-based classification model, which is able to determine whether the subimage is dominated by visible wave signatures (i.e., valid subimage) or rain echoes (i.e., invalid subimage). If all the 15 subimages in one radar image are identified as invalid subimages, this radar image will be discarded from wave estimation as well. The detailed procedures for texture feature extraction and subimage classification are introduced as follows.

1) Feature Extraction: The gray-level co-occurrence matrix (GLCM)-based method [29] that reflects the correlation characteristic of image grayscale space is an efficient texture analysis approach and used here for feature extraction from each subimage. First, an $L \times L$ sliding window is applied to the subimage. In each window, the pixels with the maximum and minimum intensities in the window are set as gray level 15 and gray level 0, respectively. Then, other pixels within the window are scaled to the integers between 0 and 15 based on the min–max feature scaling. Next, the GLCMs are formed from each pixel-intensity-scaled window as

$$P_\Delta^d = \begin{bmatrix} P_\Delta^d(0,0) & P_\Delta^d(0,1) & \cdots & P_\Delta^d(0,15) \\ P_\Delta^d(1,0) & P_\Delta^d(1,1) & \cdots & P_\Delta^d(1,15) \\ \vdots & \vdots & \ddots & \vdots \\ P_\Delta^d(15,0) & P_\Delta^d(15,1) & \cdots & P_\Delta^d(15,15) \end{bmatrix}. \quad (1)$$

The element (denoted as $P_\Delta^d(i,j)$) of the GLCM indicates the number of appearance times of the pair of pixels, which have intensities of i and j ($i, j = 0, 1, 2\dots, 15$) with a distance d along direction Δ. The Chebyshev distance, which is used to calculate the distance (d) between two pixel positions (x_1, y_1) and (x_2, y_2) in this study, is equal to $\max(\text{abs}(x_1 - x_2), \text{abs}(y_1 - y_2))$. The directional relationships of pixel pairs are shown in Fig. 5:

1) $\Delta = 1$ (in 0° direction);
2) $\Delta = 2$ (in 45° direction);
3) $\Delta = 3$ (in 90° direction);
4) $\Delta = 4$ (in 135° direction).

Since for a certain distance d, each direction Δ can be chosen to create one GLCM, four GLCMs can be generated in each sliding window.

Finally, the feature vector is constructed based on the statistics of GLCMs. In [29], 14 statistics can be calculated from the GLCM. In this study, four of them, i.e., contrast (denoted as Con), homogeneity (denoted as H), correlation (denoted as Cor), and energy (denoted as E), are selected and calculated for each GLCM, respectively, as

$$\text{Con}_\Delta = \sum_i \sum_j (i-j)^2 P_\Delta^d(i,j) \quad (2)$$

$$H_\Delta = \sum_i \sum_j \frac{1}{1 + |i-j|} P_\Delta^d(i,j) \quad (3)$$

$$\text{Cor}_\Delta = \sum_i \sum_j \frac{(i - \mu_i)(j - \mu_j) P_\Delta^d(i,j)}{\sigma_i \sigma_j} \quad (4)$$

where μ and σ are the mean and standard deviation of the GLCM, respectively:

$$\mu_i = \sum_i \sum_j i P_\Delta^d(i,j) \quad (5)$$

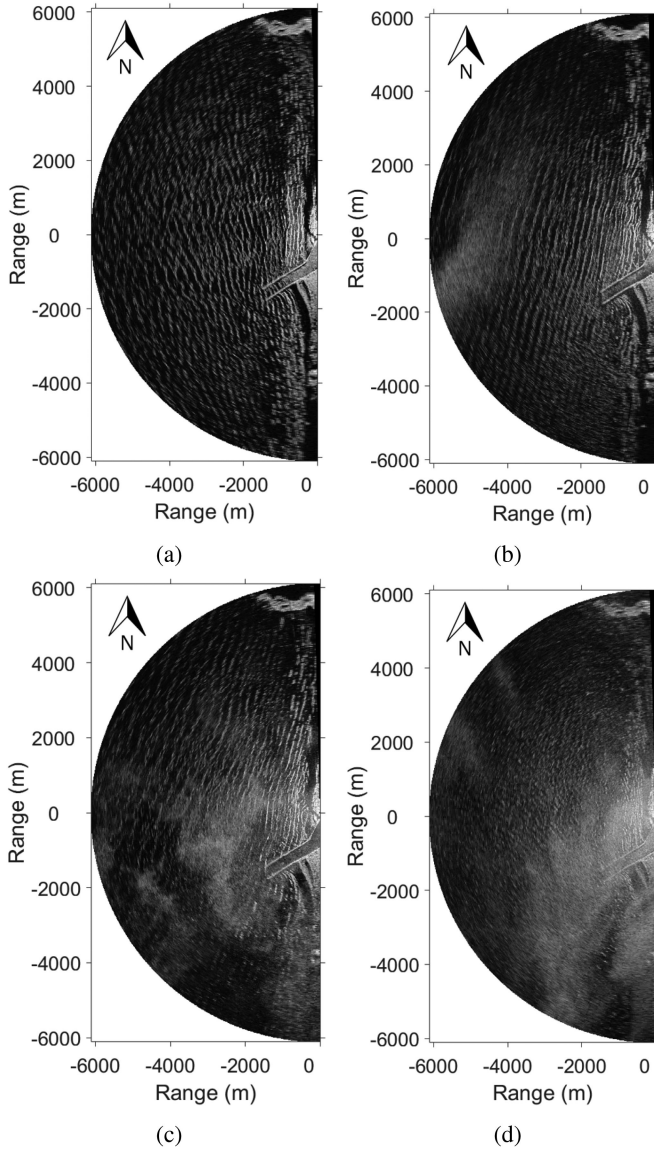$$\mu_j = \sum_i \sum_j j P_\Delta^d(i,j) \quad (6)$$

Fig. 3. Radar images obtained under different simultaneous rainfall intensities: (a) rainless, (b) 1.5-mm/h rain rate, (c) 3.0-mm/h rain rate, and (d) 9.1-mm/h rain rate.

Fig. 4. Selection of 15 subimages (outlined in red) in the radar image.
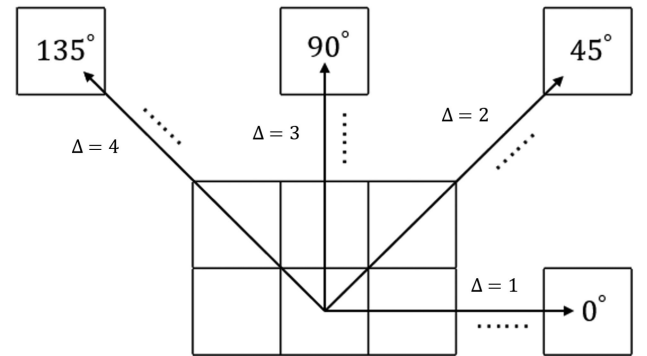
Fig. 5. Pixel pairs in four directions with same Chebyshev distance.

$$\sigma_i^2 = \sum_i \sum_j P_\Delta^d(i,j)(i - \mu_i)^2 \tag{7}$$

$$\sigma_j^2 = \sum_i \sum_j P_\Delta^d(i,j)(j - \mu_j)^2. \tag{8}$$

Also, the energy can be expressed as

$$E_\Delta = \sum_i \sum_j P_\Delta^d(i,j)^2. \tag{9}$$

In addition, the mean and standard deviation of each feature are calculated over four directions and composed as an 8-D feature vector for each sliding window. The reason why these features are selected for analysis will be illustrated in Section IV. The size (L) of the sliding window and the distance (d) between pixel pairs along four directions are set as 9 and 1, respectively,
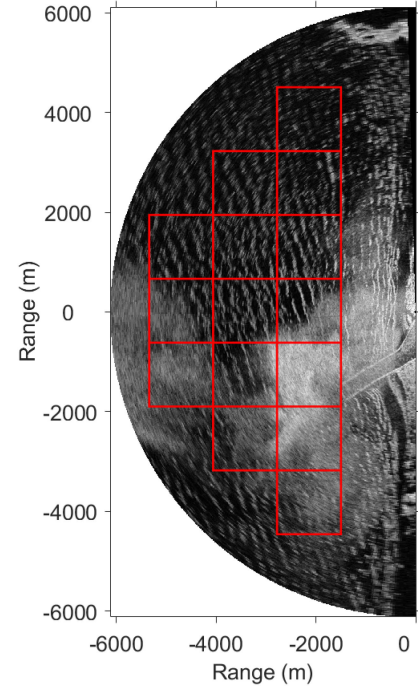
for the method used in this study. Then, for each subimage, the 8-D features of all sliding windows are combined together as one feature vector. Thus, in each subimage ($P \times P$ in pixels), the number of sliding windows (denote as W) can be calculated as $W = (P - L + 1)^2$. In order to facilitate the computation of feature vectors, all the subimages are resized into 100×100 pixels using bicubic interpolation [30]. Therefore, 8486 sliding windows can generate a feature vector with 67 712 elements in each subimage.

2) Random Forest Classification: After obtaining the texture features for all the subimages in each image, the random-forest-based classification method is used to identify the valid subimages. Random forest [31] is an ensemble learning algorithm and can be used for both classification (in this section) as well as regression, which consists of a large number of decision trees. The ensemble method is a technique that combines the predictions from multiple decision tree models together to make more

accurate predictions than any individual model. The randomness of random forest is reflected from selecting a random set of features from all features and random samples from the training dataset for each decision tree.

The architecture of the random forest classifier is shown in the right block diagram in Fig. 2, which consists of three steps (i.e., bootstrapping, decision tree training, and prediction). The first is to generate one subset via bootstrapping for each decision tree. Bootstrapping is a sampling method to draw around 63.2% samples randomly from training set (i.e., D in Fig. 2) with replacement as the training subset for the decision tree [32]. Usually, a total of n training subsets (i.e., D_1, D_2, ..., D_n in Fig. 2) should be generated (i.e., n sampling times). As for the training set, all subimages from 90 radar images obtained under different rainfall intensities are first manually labeled into two types: with relatively clear wave signatures and without clear wave signatures. Then, the extracted feature vectors of these labeled subimages and their corresponding labels are combined as the training set, while the remaining radar images are used as the testing set. The involvement of many decision trees can reduce the variance efficiently, avoid overfitting, and improve generalization. Therefore, the number of sampling times is chosen as 100 (i.e., 100 subsets or decision trees).

Next, each training subset is employed to train one decision tree model based on the classification and regression tree (CART) method [33], which is able to predict classification results according to the feature difference of input training set. In each decision tree training, the square root of the number of all features is considered as the number of selected random features, which are used for decision node selection [31]. The purpose of selecting a random set of features is to reduce the correlation between each decision tree and improve the classification accuracy of each decision tree. As for the selection of optimal feature as decision node, it can be referred to the CART method [33]. After obtaining each decision tree model, every individual tree in the random forest will produce a class prediction result. Thus, each testing sample in the testing set is input into each decision tree model, and a total of 100 classification results will be generated here. Then, a majority voting scheme is applied, which means that the class with the most votes according to all decision trees' prediction results becomes the random forest classification model's final prediction.

Therefore, the valid wave regions of each radar image can be obtained using the classification method and used for wave parameters measurement. The framed red boxes in Fig. 6 are the valid subimages identified from the rain-contaminated radar image in Fig. 4.

B. Wave Direction Estimation

After obtaining the valid subimages for each radar image, the classic method for edge detection, i.e., Canny edge detection proposed in [34], is first performed on each valid subimage in order to facilitate line detection using the RT in next step. In this study, in order to outline the main texture with less computation load, each subimage used for edge detection is still
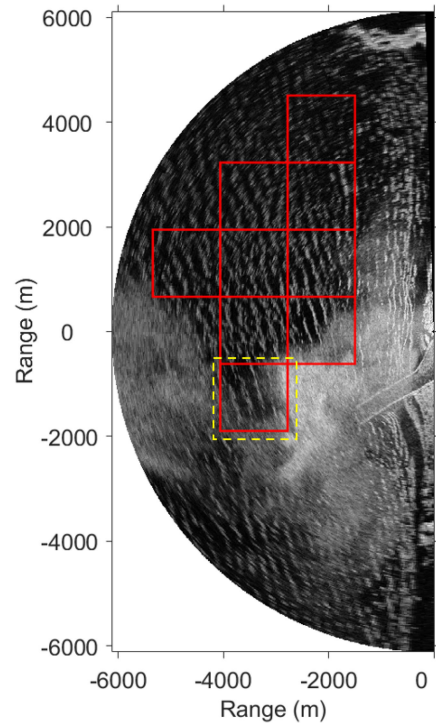

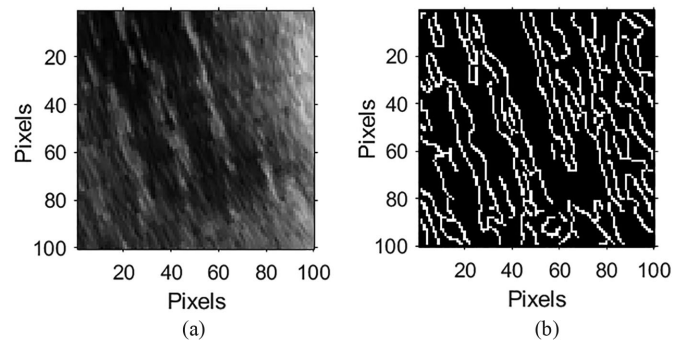Fig. 6. Valid subimages (outlined in red) identified from radar image in Fig. 4.

Fig. 7. (a) Valid subimage highlighted in yellow dashed lines in Fig. 6. (b) Detected edge image of (a).

in 100×100 pixels. An example of the edge detection result of a valid subimage [i.e., Fig. 7(a)] is presented in Fig. 7(b). Next, the dominant direction (denoted as η) of each edge image is estimated using the RT-based method. The RT [35] can be expressed as

$$f(r,\alpha) = \int \int I(x,y)\delta(r - x\cos\alpha - y\sin\alpha)dxdy \quad (10)$$

where $I(x,y)$ is the pixel intensity at location (x,y) in the edge image, δ is the Dirac delta function, r represents the distance from the center of edge image to a candidate straight line in the image, and α is the angle between the normal of the straight line and the x-axis, which is also the projection direction of the
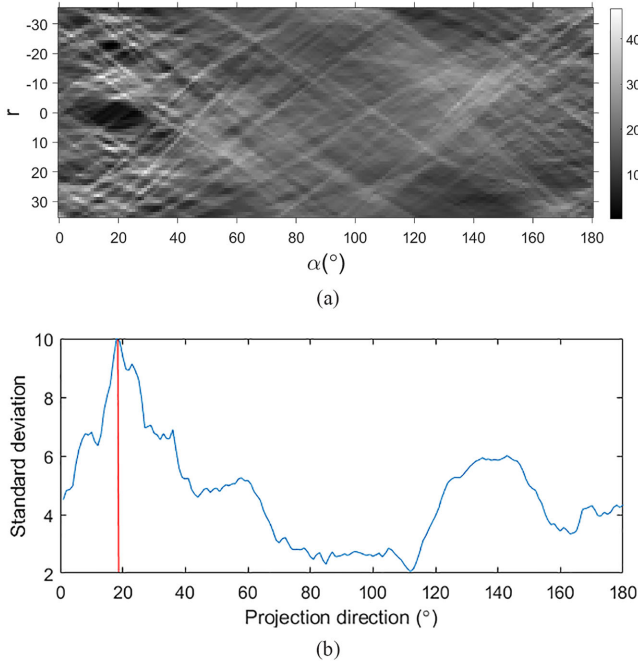
Fig. 8.   (a) RT results of all projection lines in Fig. 7(b). (b) Standard deviation of RT results as a function of projection direction.
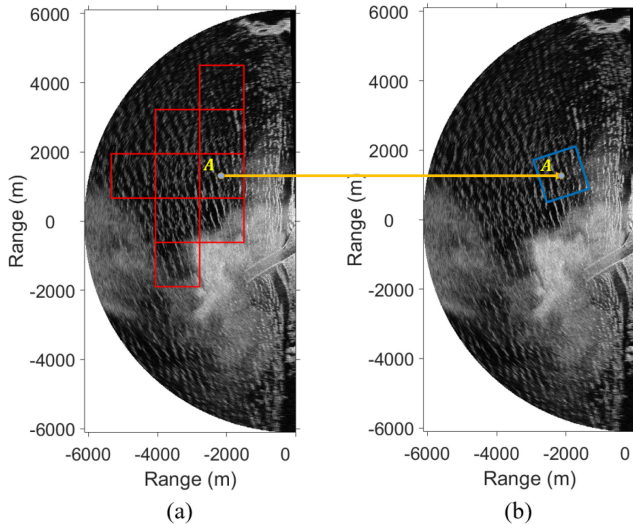

Fig. 9.   Region extraction for wave period estimation. (a) Selected valid subimage centering at A. (b) Extracted region centering at A for wave period estimation outlined in blue.

straight line. It is obvious that

$$r = x \cos \alpha + y \sin \alpha. \qquad (11)$$

The RT for α and r in (10) represents the integral of the intensity of all the pixels on a line which is in the direction α and at a distance r relative to the image center, i.e., each point in the RT domain corresponds to a straight line in image space. As for the detected edge image, it can be found that one texture line with high gray level and a distance r as well as direction α relative to the edge image center will generate a bright point at (α, r) in the

RT domain. On the contrary, the texture line with low gray level will generate a dark point in the RT domain. Thus, the pixels in the RT domain image in the corresponding texture line projection direction will display the largest intensity value variation. The standard deviation of the pixel intensities in each projection direction (α) of transformed result in the Radon domain can be calculated, and the direction with peak standard deviation value can be considered as the texture dominant direction (η).

To reduce computation, for an edge image that contains l pixels in each side, only the projection lines that have at least $l/\sqrt{2}$ pixels are used for the RT, which means the absolute value of applicable distance r is less than $l/(2\sqrt{2})$ pixels. Based on this criterion, the RT result of Fig. 7(b) is presented in Fig. 8(a). Besides, the standard deviation of the pixel intensities in each project direction (α) of Fig. 8(a) is calculated and shown in Fig. 8(b). It can be observed that the texture dominant direction of Fig. 7(a) is $18°$. Furthermore, for each radar image, the standard deviations of RT results obtained from all valid subimages are averaged for each projection direction, and the direction with the maximum averaged standard deviation is selected as a rough estimation direction (denoted as ϕ). Next, by comparing η with ϕ, only those subimages with η being within $\pm 10°$ of ϕ are selected, and the median value of η associated with the selected subimages is regarded as the final texture dominant direction (denoted as γ) of one radar image [5]. It should be noted that η and γ should be converted to β and θ, which are measured with reference to the true North.

C. Wave Period Estimation

The steps for wave period estimation are illustrated as follows. As shown in Fig. 9(a), the valid subimage with its dominant wave direction (β) closest to the estimated wave direction (θ) from the corresponding radar image is selected. Then, a (256 × 256)-pixel region that centers at the original subimage center with two sides aligning with the estimated wave direction is selected for wave period estimation, as depicted in Fig. 9(b). Similar to the subimage selection step, the GLCM-based method is also used for texture feature extraction. In this method, the size of the sliding window is 59×59 pixels, and the distance between the pixel pairs is selected as 4. Since the wave period is related to the spacing between the wave signatures [36], if the window size is too small, the sliding window cannot include sufficient wave signatures and, therefore, cannot reflect accurate spacing between the wave signatures. In contrast, the number of generated texture features would be less if a larger window is used because the number of available sliding windows will decrease. As for the distance between the pixel pairs, the value of 4 is chosen to ensure that it is large enough to capture most variations of pixel intensities between adjacent wave crests and troughs. If the distance value is too small, the variations between pixel pairs may not be observed, while a very large distance will cause the fact that the feature obtained does not represent the variation between adjacent wave crests and troughs. Therefore, in each 256 × 256 subimage, 39 204 sliding windows can generate 313 632 feature values to obtain one feature vector.
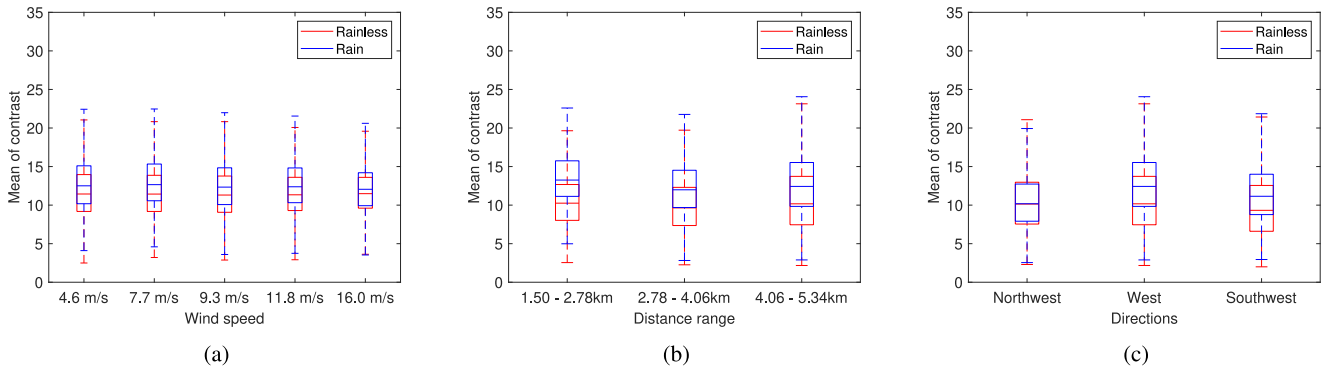
Fig. 10.   Box plots of the mean contrast distributions for different (a) wind speeds, (b) ranges, and (c) directions.
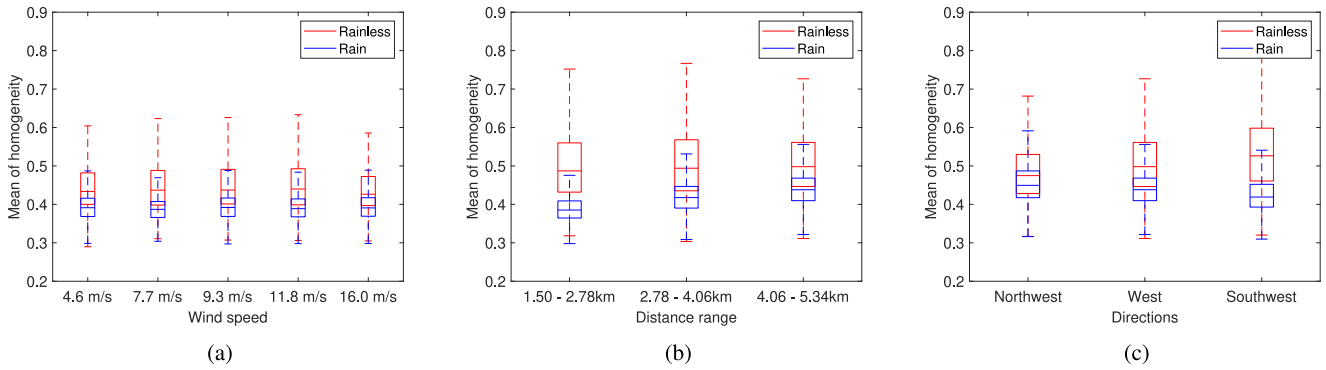

Fig. 11.   Box plots of the mean homogeneity distributions for different (a) wind speeds, (b) ranges, and (c) directions.
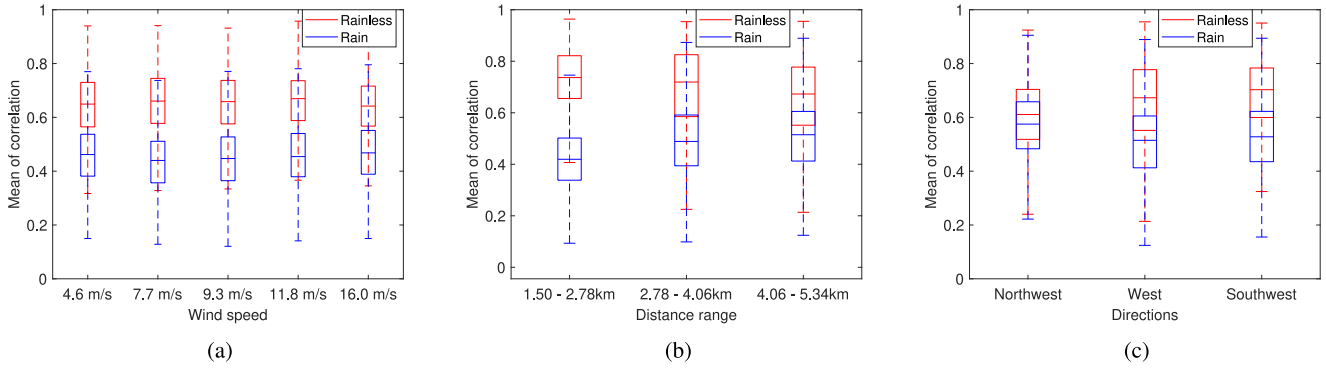

Fig. 12.   Box plots of the mean correlation distributions for different (a) wind speeds, (b) ranges, and (c) directions.
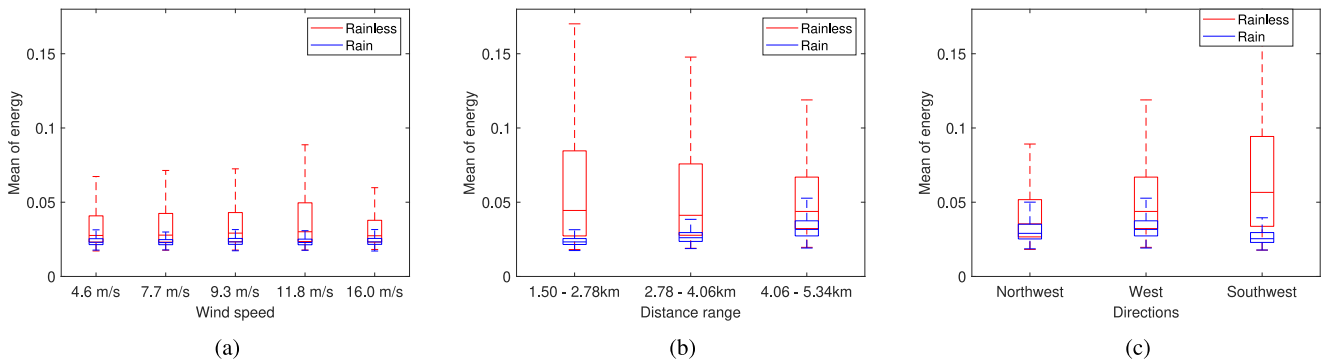

Fig. 13.   Box plots of the mean energy distributions for different (a) wind speeds, (b) ranges, and (c) directions.
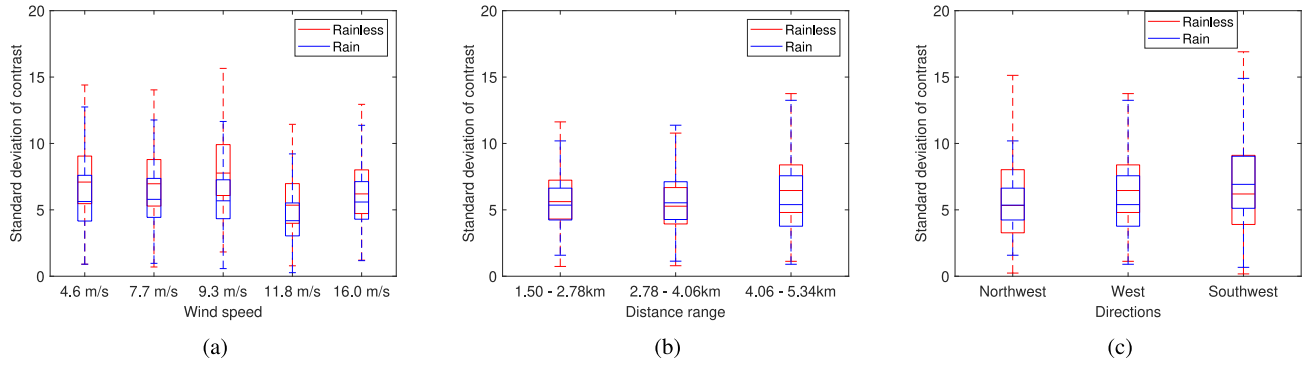
Fig. 14. Box plots of the standard deviation distribution of contrast for different (a) wind speeds, (b) ranges, and (c) directions.
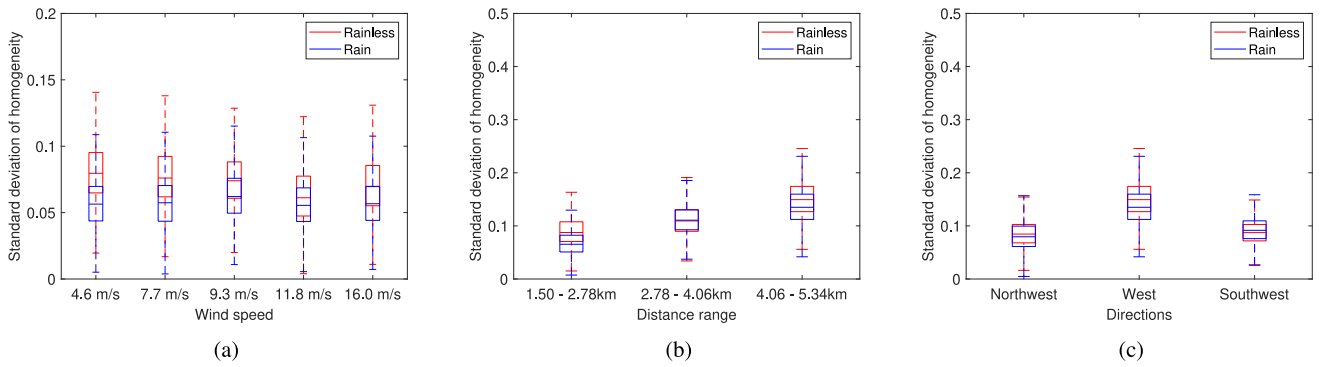

Fig. 15. Box plots of the standard deviation distribution of homogeneity for different (a) wind speeds, (b) ranges, and (c) directions.
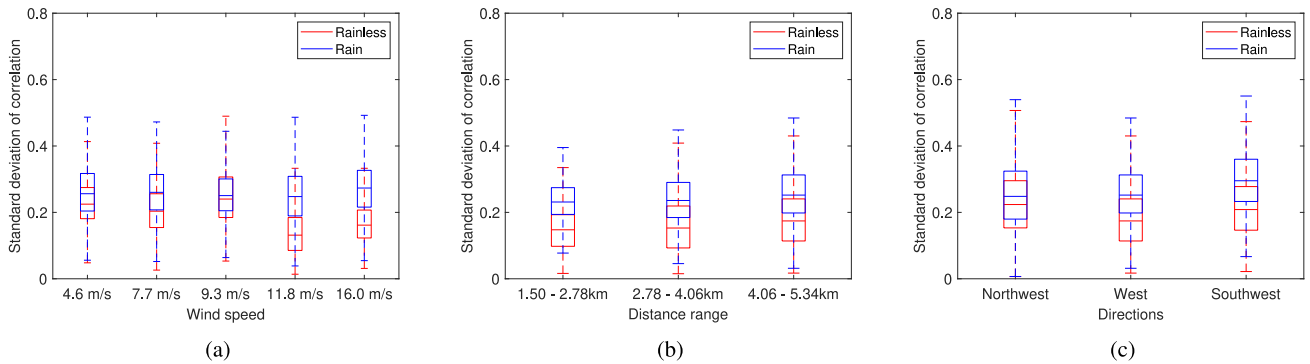

Fig. 16. Box plots of the standard deviation distribution of correlation for different (a) wind speeds, (b) ranges, and (c) directions.

After obtaining the texture features, the random-forest-based regression algorithm [37] is used to train the wave period estimation model. Although the main training steps of the random-forest-based regression model are the same as those of the aforementioned random-forest classification algorithm, the goal of the proposed regression model is to obtain the smallest difference between the actual data value (buoy-measured wave period in this study) and the radar-derived wave period. Besides, the number of randomly selected features for training of each decision tree is one-third of all features [31]. Moreover, the output at each leaf of the decision tree is wave period. In this study, the final predicted wave period of each radar image equals

the average of the predicted results generated by 100 trained regression models.

IV. EXPERIMENTAL RESULTS

In this study, the radar-derived estimation results are analyzed under four rainfall intensity levels, i.e., rainless, light rain, moderate rain, and heavy rain. According to the Manual of Surface Weather Observations [38], the range of rain rates for each level is:

1) rainless: zero rain rate;
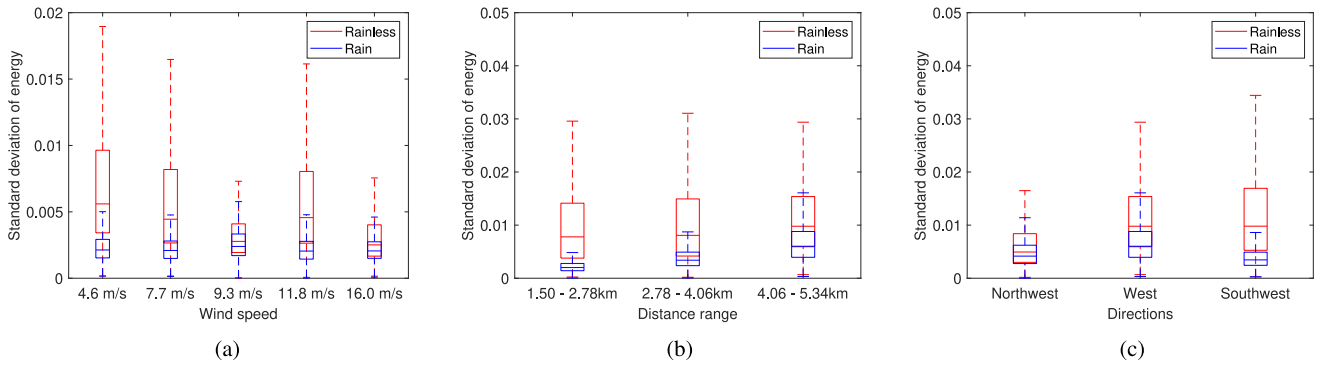2) light rain: nonzero rain rates less than 2.5 mm/h;

Fig. 17.   Box plots of the standard deviation distribution of energy for different (a) wind speeds, (b) ranges, and (c) directions.
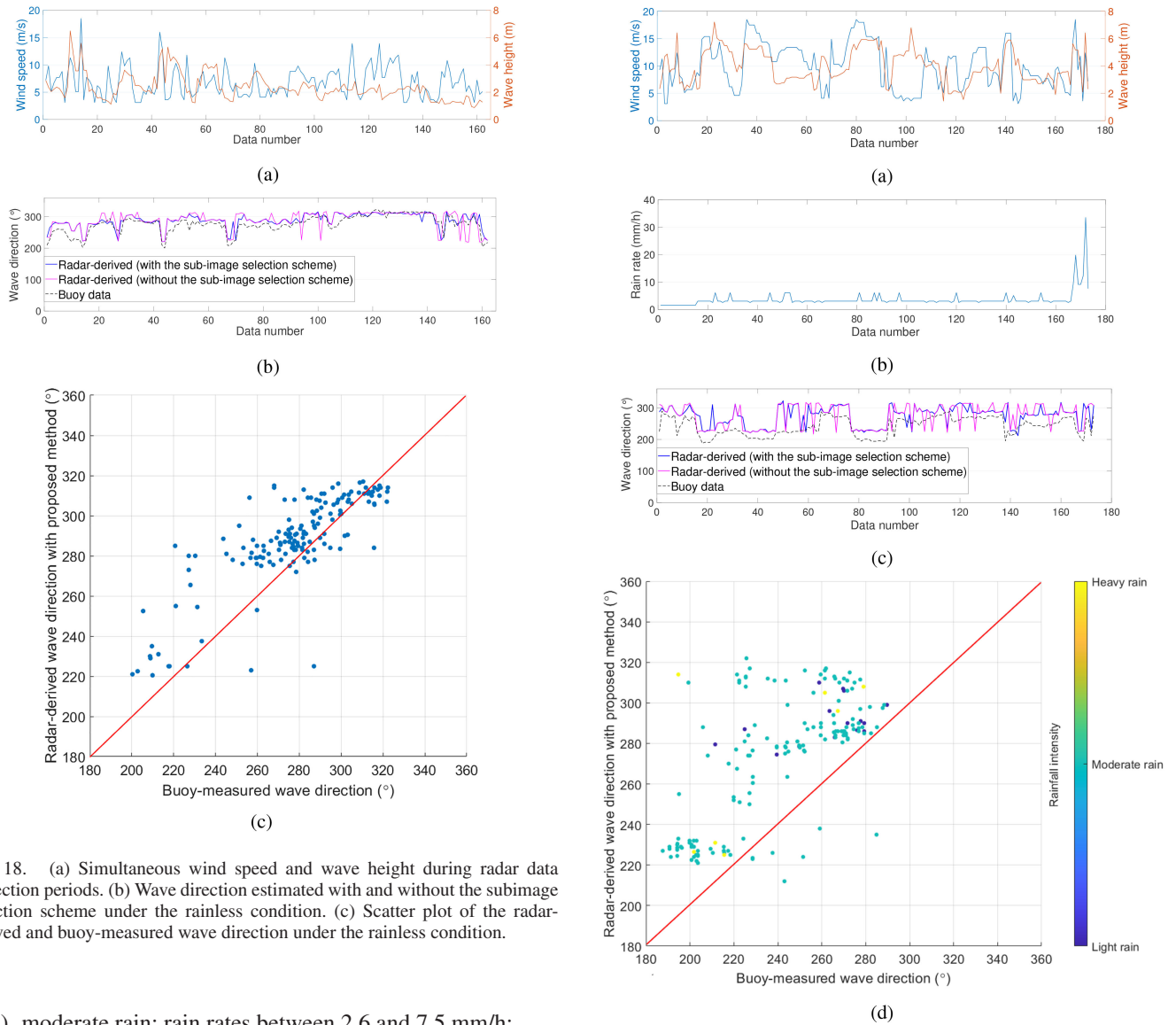
Fig. 18.   (a) Simultaneous wind speed and wave height during radar data collection periods. (b) Wave direction estimated with and without the subimage selection scheme under the rainless condition. (c) Scatter plot of the radar-derived and buoy-measured wave direction under the rainless condition.

Fig. 19.   (a) Simultaneous wind speed and wave height during radar data collection periods. (b) Simultaneous rain rates during radar data collection periods. (c) Wave direction estimated with and without the subimage selection scheme under rainfall conditions. (d) Scatter plot of the radar-derived and buoy-measured wave direction under different rainfall intensities.

3) moderate rain: rain rates between 2.6 and 7.5 mm/h;
4) heavy rain: rain rates between 7.6 and 50 mm/h.

Besides, in order to validate the effectiveness of the subimage selection scheme for rain effect mitigation, the proposed wave direction and wave period estimation algorithms without

Fig. 20.   Scatter plots of radar-derived wave period with the subimage selection scheme and buoy-measured wave period under (a) rainless condition, (b) light rain condition, (c) moderate rain condition, and (d) heavy rain condition.
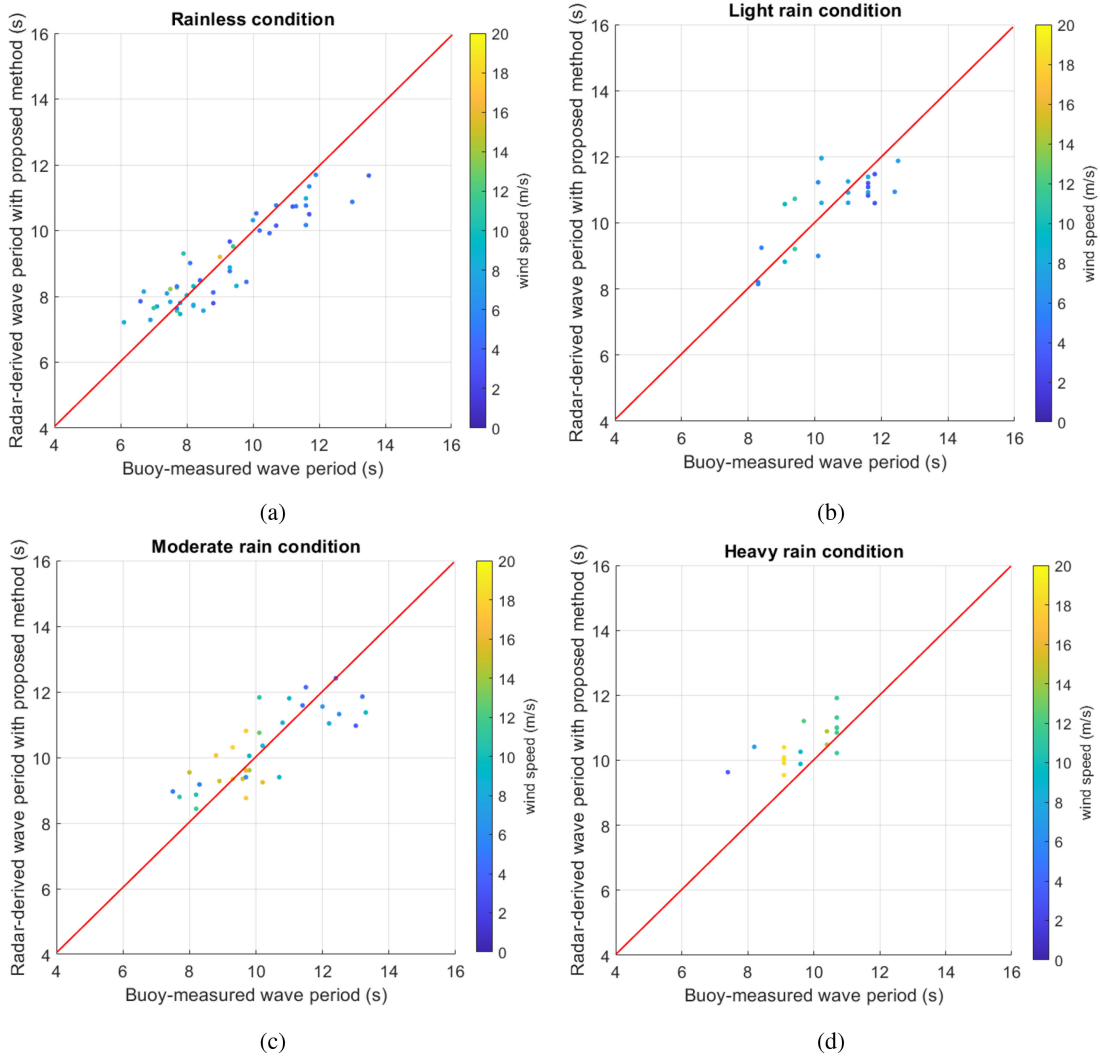
applying the subimage selection scheme are also implemented for comparison, in which the 15 subimages in each radar images are all used for wave parameter estimation without exclusion.

A. Influence of Rain on Extracted Features

In order to verify the effectiveness of classifying between rainless and rainy images using these four features (Con, H, Cor, and En) from the GLCM, the mean and standard deviation of each feature calculated from rainless and rainy subimages for different wind speeds, observation ranges, and observation directions are compared with each other, which are shown in the box plots in Figs. 10–17. In each figure, the red and blue box plots represent the results calculated under rainless and rainy conditions, respectively. From Figs. 10–13, it can be observed that the medians of mean contrast under the rainless condition are generally lower than that obtained under the rainy condition. In contrast, the medians of mean homogeneity, correlation, and energy under the rainless condition are all larger than that obtained

under the rainy condition. From Figs. 14–17, it can be noticed that most of the median standard deviations calculated from the contrast, homogeneity, and energy under the rainless condition are larger than that obtained under the rainy condition. On the other hand, the median standard deviations calculated from correlation under the rainless condition are smaller than that obtained under the rainy condition. According to the difference of the mean and standard deviation distributions of each feature under the rainless and rainy conditions, it can be concluded that values of these image features will be influenced by rain. Thus, it is feasible to extract the mean and variance of these features as feature vectors to train the classification model.

B. Wave Direction Result Analysis

Table II shows the root-mean-square errors (RMSEs) between the radar-derived and the buoy-measured wave directions. From Table II, it can be observed that the proposed subimage selection scheme effectively improves estimation accuracy by
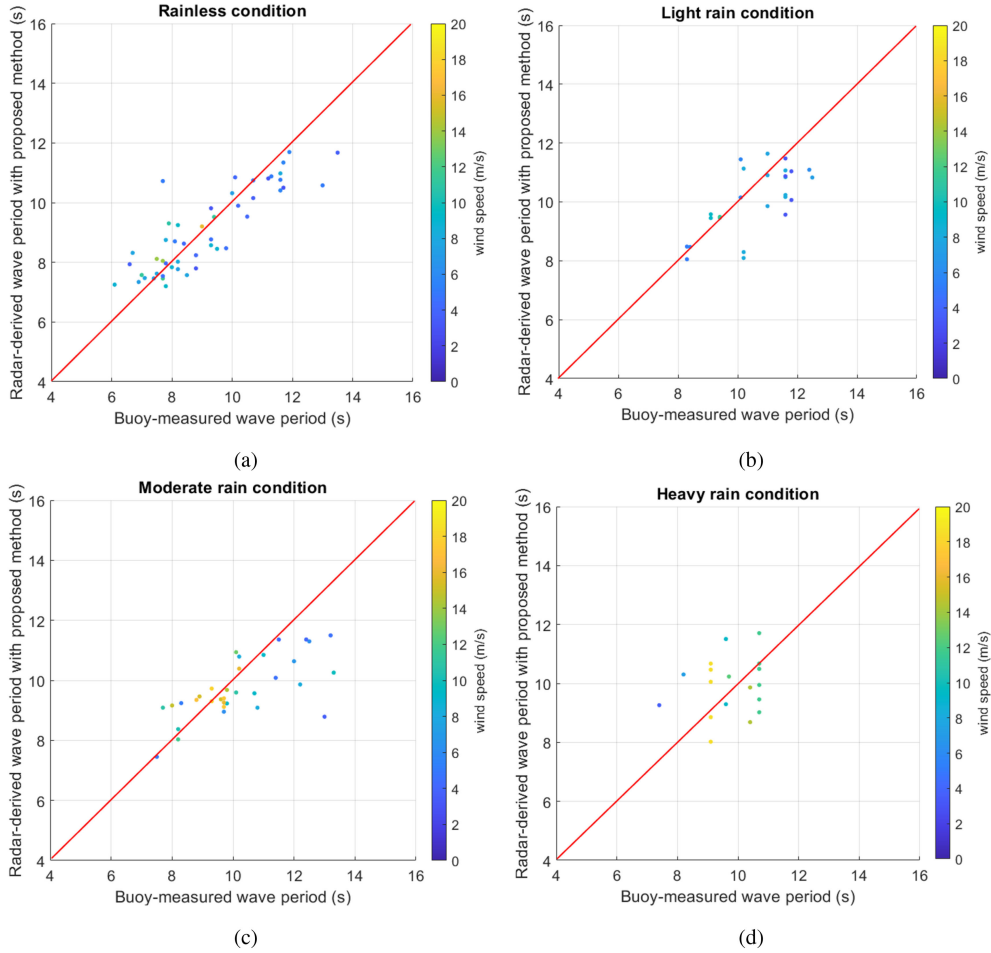
Fig. 21. Scatter plots of radar-derived wave period without the subimage selection scheme and buoy-measured wave period under (a) rainless condition, (b) light rain condition, (c) moderate rain condition, and (d) heavy rain condition.

TABLE II
RMSES OF WAVE DIRECTION ESTIMATION UNDER DIFFERENT
RAINFALL INTENSITIES

Rainfall intensity level	with sub-image selection scheme	without sub-image selection scheme
Rainless	19.7°	26.6°
Light rain	34.7°	40.7°
Moderate rain	39.8°	44.7°
Heavy rain	51.9°	52.9°

reducing the RMSEs of estimation results under four rain intensity levels. Also, when rain level increases, the improvement is less. It should be noted that under the heavy rain condition, the difference between RMSEs of wave direction is only 1°, which may be associated with the error of the buoy. However, as shown in Fig. 19(a) and (b), most heavy rain samples are obtained under wind speeds higher than 10 m/s. According to our previous research [39], the generated surface roughness might be dominated by wind force under high wind speeds, and rain may only cause additional radar backscatter instead of blurring surface wave signatures significantly. As a consequence, wave signatures may be visible in the radar images under the heavy rain condition. In Table I, the small difference between RMSEs

of wave direction under heavy rain is reasonable. In addition, the number of images obtained under heavy rain is much less than those obtained under light rain and moderate rain. Therefore, more image data obtained under the heavy rain condition should be used to further evaluate the effectiveness of the proposed method in the future work.

Figs. 18 and 19 are presented in order to further analyze the wave direction estimation results under rainless and rainy conditions. Specifically, Figs. 18(a) and 19(a) show the simultaneous wind speed and wave height information of each sample. It can be observed from Fig. 18(b) that a few relatively large deviations between radar-derived results and buoy measurements appear when the subimage selection scheme is not used under the rainless condition. These deviations are mainly caused by estimation from some low-backscatter regions in the radar images. From Fig. 19(c), it can be found that there are many relatively large deviations between radar-derived results and buoy measurements if the subimage selection scheme is not applied. This is mainly caused by estimation from the regions severely contaminated by rain. In contrast, the subimage selection scheme leads to a better performance in wave direction estimation, proving that this method can effectively mitigate the rainfall effect on estimation. As for Figs. 18(c) and 19(d), it can be found

TABLE III
RMSEs of Wave Period Estimation Under Different
Rainfall Intensities

Rainfall intensity level	With sub-image selection scheme	Without sub-image selection scheme
Rainless	0.80 s	0.93 s
Light rain	0.88 s	1.10 s
Moderate rain	0.98 s	1.28 s
Heavy rain	1.04 s	1.24 s

that the deviation of estimated wave direction increases with the increase of rainfall intensities. Under the rainy condition, the wave signatures may be still affected by rain even the texture is clear in the subimage identified by the selection scheme. Besides, another reason for the large difference between the wave direction estimated from the radar images and buoy data is that the buoy site is far away from the coastal radar system and is not within the radar coverage range. Moreover, there is no obvious relationship between the wave direction estimation accuracy and wind speed as well as wave height.

C. Wave Period Result Analysis

Considering that the number of testing samples with light rain and heavy rain is small, so more than one valid subimages are extracted from light and heavy radar images to expand the data for wave period estimation. According to Dobbin and Simon [40], the ideal amount of the training set is 40–80% of the whole dataset. Thus, the whole dataset is split into 70% for training and 30% for testing in this experiment. The training set is composed of both rainless and rain-contaminated subimages. Besides, the proposed method with and without the subimage selection scheme is tested. As for the method without using the subimage selection scheme, the subimages for wave period estimation are selected along the estimated wave direction in each radar image.

Table III shows the RMSEs between the radar-derived and buoy-measured wave periods. It can be observed that the subimage selection scheme helps decrease the RMSEs by 0.13, 0.20, 0.30, and 0.20 s under four rainfall intensity levels, respectively. It can be found that the RMSE of the wave period under the moderate rain condition is the largest when the subimage selection scheme is not used. As mentioned earlier, wave signatures may still be visible in the radar images under the heavy rain condition. In contrast, those moderate rain samples obtained under low wind speeds will be dominated by rain echoes with little visible wave signatures; hence, the estimation accuracy of those samples will decrease, and the corresponding RMSE is relatively large.

Figs. 20 and 21 show the comparison of radar-derived and buoy-measured wave periods under different rainfall intensities. Moreover, the color intensity at each point indicates the wind speed. From Figs. 20 and 21, it can be found that the method without using the subimage selection scheme generated larger deviations than that with the subimage selection scheme. Thus, it shows that the subimage selection scheme can also efficiently mitigate the rain effect on wave period estimation. Furthermore, it also can be observed that the estimated deviation still increases with the increase in rainfall intensities. Moreover, there is no obvious relationship between the wave period estimation accuracy and the wind speed.

V. Conclusion

In this article, the influence of rainfall intensity on wave direction and period estimation from *X*-band marine radar images is analyzed. First, a random-forest-based classification method for identifying the valid subimages with visible wave signatures is proposed to reduce rain effect. Wave direction is estimated from the selected valid subimages of each radar image by performing an RT-based algorithm, while a novel method based on the texture feature extraction and a random-forest-based regression model is proposed for wave period estimation. Experimental results show that the subimage selection scheme plays a significant role in reducing wave direction and wave period estimation errors under different rain conditions. In addition, it has also been observed that as the rain rate increases, the influence of rain on wave parameter estimation tends to be more severe as well. Future work will focus on the analysis of rain influence on wave height measurement [41] from rain-contaminated *X*-band marine radar images.

References

[1] X. Liu, W. Huang, and E. W. Gill, "Wave height estimation from shipborne X-band nautical radar images," *J. Sens.*, vol. 2016, 2016, Art. no. 1078053.
[2] B. Lund, H. C. Graber, and R. Romeiser, "Wind retrieval from shipborne nautical X-band radar data," *IEEE Trans. Geosci. Remote Sens.*, vol. 50, no. 10, pp. 3800–3811, Oct. 2012.
[3] H. Dankert, J. Horstmann, and W. Rosenthal, "Ocean wind fields retrieved from radar-image sequences," *J. Geophys. Res.*, vol. 108, no. C11, pp. 2150–2152, 2003.
[4] I. R. Young, W. Rosenthal, and F. Ziemer, "A three-dimensional analysis of marine radar images for the determination of ocean wave directionality and surface currents," *J. Geophys. Res.-Oceans*, vol. 90, no. C1, pp. 1049–1059, 1985.
[5] B. Lund, H. C. Graber, J. Xue, and R. Romeiser, "Analysis of internal wave signatures in marine radar data," *IEEE Trans. Geosci. Remote Sens.*, vol. 51, no. 9, pp. 4840–4852, Sep. 2013.
[6] J. C. Nieto-Borge, K. Hessner, and P. Jarabo-Amores, "Signal-to-noise ratio analysis to estimate ocean wave heights from X-band marine radar image time series," *IET Radar, Sonar Navigat.*, vol. 2, no. 1, pp. 35–41, 2008.
[7] J. C. Nieto-Borge and C. Guedes-Soares, "Analysis of directional wave fields using X-band navigation radar," *Coastal Eng.*, vol. 40, no. 4, pp. 375–391, 2000.
[8] R. Gangeskar, "Ocean current estimated from X-band radar sea surface, images," *IEEE Trans. Geosci. Remote Sens.*, vol. 40, no. 4, pp. 783–792, Apr. 2002.
[9] C. M. Senet, J. Seemann, and F. Ziemer, "The near-surface current velocity determined from image sequences of the sea surface," *IEEE Trans. Geosci. Remote Sens.*, vol. 39, no. 3, pp. 492–505, Mar. 2001.
[10] C. Shen, W. Huang, E. W. Gill, R. Carrasco, and J. Horstmann, "An algorithm for surface current retrieval from X-band marine radar images," *Remote Sens.*, vol. 7, no. 6, pp. 7753–7767, 2015.
[11] W. Huang, X. Liu, and E. Gill, "Ocean wind and wave measurements using X-band marine radar: A comprehensive review," *Remote Sens.*, vol. 9, no. 12, 2017, Art. no. 1261.

[12] Z. Lu, B. Lv, L. Li, and S. Guo, "Research on rainfall identification based on the echo differential value from X-band navigation radar image," in *Proc. IEEE Int. Conf. Mechatronics Autom.*, 2019, pp. 2347–2351.

[13] R. F. Contreras and W. J. Plant, "Surface effect of rain on microwave backscatter from the ocean: Measurements and modeling," *J. Geophys. Res. Oceans*, vol. 111, no. C8, pp. 1–18, 2006.

[14] X. Chen and W. Huang, "Identification of rain and low-backscatter regions in X-band marine radar images: An unsupervised approach," *IEEE Trans. Geosci. Remote Sens.*, vol. 58, no. 6, pp. 4225–4236, Jun. 2020.

[15] J. Shen, Y. Li, Y. Dai, and S. Wang, "Identification and suppression of rain interference on X-band radar images," *Opt. Precis. Eng.*, vol. 20, no. 8, pp. 1846–1853, 2012.

[16] X. Chen, W. Huang, C. Zhao, and Y. Tian, "Rain detection from X-band marine radar images: A support vector machine-based approach," *IEEE Trans. Geosci. Remote Sens.*, vol. 58, no. 3, pp. 2115–2123, Mar. 2020.

[17] Y. Liu, W. Huang, and E. W. Gill, "Analysis of the effects of rain on surface wind retrieval from X-band marine radar images," in *Proc. 2014 Oceans - St John's*, 2014, pp. 1–4.

[18] W. Huang, X. Liu, and E. W. Gill, "An empirical mode decomposition method for sea surface wind measurements from X-band nautical radar data," *IEEE Trans. Geosci. Remote Sens.*, vol. 55, no. 11, pp. 6218–6227, Nov. 2017.

[19] X. Chen, W. Huang, and G. Yao, "Wind speed estimation from X-band marine radar images using support vector regression method," *IEEE Trans. Geosci. Remote Sens. Lett.*, vol. 15, no. 9, pp. 1312–1316, Sep. 2018.

[20] Z. Chen, Y. He, B. Zhang, and Y. Ma, "A method to correct the influence of rain on X-band marine radar image," *IEEE Access*, vol. 5, pp. 25576–25583, 2017.

[21] *Yaquina Bay and River Marine Chart*, Apr. 9, 2021. [Online]. Available: http://www.gpsnauticalcharts.com/main/us18581_p1792-yaquina-bay-and-river-nautical-chart.html

[22] W. Huang, Y. Liu, and E. Gill, "Texture-analysis-incorporated wind parameters extraction from rain-contaminated X-band nautical radar images," *Remote Sens.*, vol. 9, no. 2, 2017, Art. no. 166.

[23] X. Liu, W. Huang, and E. W. Gill, "An algorithm for estimation of wave parameters from X-band marine radar images," in *Proc. IEEE Radar Conf.*, 2018, pp. 95–99.

[24] R. Gangeskar, "An adaptive method for estimation of wave height based on statistics of sea surface images," in *Proc. IEEE Int. Geosci. Remote Sens. Symp.*, Honolulu, HI, USA, 2000, vol. 1, pp. 255–259.

[25] R. Gangeskar, "Wave height derived by texture analysis of X-band radar sea surface images," in *Proc. IEEE Int. Geosci. Remote Sens. Symp.*, Honolulu, HI, USA, 2000, vol. 7, pp. 2952–2959.

[26] L. Cornejo-Bueno, J. Nieto-Borge, E. Alexandre, K. Hessner, and S. Salcedo-Sanz, "Accurate estimation of significant wave height with support vector regression algorithms and marine radar images," *Coastal Eng.*, vol. 114, pp. 233–243, 2016.

[27] R. Vicen-Bueno, C. Lido-Muela, and J. Nieto-Borge, "Estimate of significant wave height from non-coherent marine radar images by multilayer perceptrons," *EURASIP J. Adv. Signal Process.*, vol. 2012, 2012, Art. no. 84.

[28] X. Chen and W. Huang, "Gaussian process regression for estimating wind speed from X-band marine radar images," in *Proc. OCEANS 2018 MTS/IEEE Charleston*, 2018, pp. 1–4.

[29] R. M. Haralick, K. Shanmugam, and I. Dinstein, "Textural features for image classification," *IEEE Trans. Syst., Man, Cybern.*, vol. SMC-3, no. 6, pp. 610–621, Nov. 1973.

[30] R. Keys, "Cubic convolution interpolation for digital image processing," *IEEE Trans. Acoust. Speech Signal Process.*, vol. 29, no. 6, pp. 1153–1160, Dec. 1981.

[31] L. Breiman, "Random forests," *Mach. Learn.*, vol. 45, no. 1, pp. 5–32, 2001.

[32] B. Efron and R. Tibshirani, "Improvements on cross-validation: The 632 bootstrap method," *J. Amer. Statist. Assoc.*, vol. 92, no. 438, pp. 548–560, 1997.

[33] L. Breiman, J. H. Friedman, R. A. Olshen, and C. J. Stone, *Classification and Regression Trees*. Kennett Square, PA, USA: Wadsworth International, 1984.

[34] J. Canny, "A computational approach to edge detection," *IEEE Trans. Pattern Anal. Mach. Intell.*, vol. PAMI-8, no. 6, pp. 679–698, Nov. 1986.

[35] J. Radon, "Über die bestimmung von funktionen durch ihre integralwerte längs gewisser mannigfaltigkeiten," *Math. Phys. Klasse*, vol. 69, pp. 262–277, 1917.

[36] Z. Chen, Y. He, B. Zhang, Z. Qiu, and B. Yin, "A new algorithm to retrieve wave parameters from marine X-band radar image sequences," *IEEE Trans. Geosci. Remote Sens.*, vol. 52, no. 7, pp. 4083–4091, Jul. 2014.

[37] J. Xie, J. Zhang, X. Xie, Z. Bi, and Z. Li, "Ensemble of bagged regression trees for concrete dam deformation predicting," *IOP Conf. Ser.: Earth Environ. Sci.*, vol. 376, 2019, Art. no. 012040.

[38] *Manual of Surface Weather Observations Standards*, 8th ed., Environment and Climate Change Canada, Gatineau, QC, Canada, 2019.

[39] Y. Wang and W. Huang, "An algorithm for wind direction retrieval from X-band marine radar images," *IEEE Geosci. Remote. Sens. Lett.*, vol. 13, no. 2, pp. 252–256, Feb. 2016.

[40] K. Dobbin and R. Simon, "Optimally splitting cases for training and testing high dimensional classifiers," *BMC Med. Genomics*, vol. 4, no. 31, 2011, Art. no. 31.

[41] W. Huang, E. W. Gill, and J. An, "Iterative least-squares-based wave measurement using X-band nautical radar," *IET Radar Sonar Navigat.*, vol. 8, no. 8, pp. 853–863, 2014.

Zhiding Yang (Student Member, IEEE) received the B.Eng. degree in electrical information engineering from the Wuhan University of Science and Technology, Wuhan, China, in 2018. He is currently working toward the M.Eng. degree in electrical engineering with the Memorial University of Newfoundland, St. John's, NL, Canada.

His research interests include *X*-band marine radar ocean surface remote sensing.

Weimin Huang (Senior Member, IEEE) received the B.S., M.S., and Ph.D. degrees in radio physics from Wuhan University, Wuhan, China, in 1995, 1997, and 2001, respectively, and the M.Eng. degree in electrical engineering from the Memorial University of Newfoundland, St. John's, NL, Canada, in 2004.

From 2008 to 2010, he was a Design Engineer with Rutter Technologies, St. John's. Since 2010, he has been with the Faculty of Engineering and Applied Science, Memorial University of Newfoundland, where he is currently a Professor. He has authored more than 250 research papers. His research interests include the mapping of oceanic surface parameters via high-frequency ground wave radar, *X*-band marine radar, and global navigation satellite systems.

Dr. Huang is a Technical Program Committee Member. He served as a Technical Program Co-Chair of the IEEE Newfoundland Electrical and Computer Engineering Conference in 2012 and 2013. He is currently an Area Editor for IEEE CANADIAN JOURNAL OF ELECTRICAL AND COMPUTER ENGINEERING, an Associate Editor for IEEE ACCESS, an Editorial Board Member of *Remote Sensing*, and a Guest Editor for IEEE JOURNAL OF SELECTED TOPICS IN APPLIED EARTH OBSERVATIONS AND REMOTE SENSING. He serves as a Regular Reviewer more than 60 international journals and a Reviewer for many IEEE international conferences, such as RadarCon, International Conference on Communications, IEEE Global Communications Conference, IEEE Geoscience and Remote Sensing Society, and Oceans. He was the recipient of Postdoctoral Fellowship from the Memorial University of Newfoundland. In 2017, he was the recipient of the Discovery Accelerator Supplements Award from the Natural Sciences and Engineering Research Council of Canada. He is the recipient of the IEEE Geoscience and Remote Sensing Society 2019 Letters Prize Paper Award.

Xinwei Chen (Student Member, IEEE) was born in Guangzhou, China. He received the B.Eng. degree in information engineering from the South China University of Technology, Guangzhou, China, in 2017. He is currently working toward the Ph.D. degree in electrical engineering with the Memorial University of Newfoundland, St. John's, NL, Canada.

His research interests include *X*-band marine radar ocean surface remote sensing.